Selective manipulation of stop-bands in multi-component photonic crystals: Opals as an example

M. V. Rybin,[1] A. V. Baryshev,[1,2] A. B. Khanikaev,[2] M. Inoue,[2] K. B. Samusev,[1] A. V. Sel'kin,[1] G. Yushin,[3] and M. F. Limonov[1]

[1]*Ioffe Physico-Technical Institute, St. Petersburg 194021, Russia*

[2]*Toyohashi University of Technology, Toyohashi, Aichi 441-8580, Japan*

[3]*Department of Materials Science, Georgia Institute of Technology, Atlanta, Georgia 30332-0245, USA*

(Received 13 November 2007; revised manuscript received 20 March 2008; published 13 May 2008)

We report on a comprehensive theoretical and experimental study of stop-band switching in photonic crystals. The suggested principles of light control are based on new Bragg diffraction effects discovered in multi-component periodic structures. The described analytical approach allows a detailed study of selective switching of (*hkl*) stop-bands by varying the permittivity of the components or the lattice parameters. For two-component photonic crystals, we showed two possible switching-off regimes. In the first regime, all of the stop-bands may only be simultaneously switched off if the certain matching conditions for permittivities are satisfied. In contrast, in the second regime, one can selectively switch off a preferred stop-band by adjusting the structural parameters irrespective of the permittivity values. For multi-component crystals, the on/off switching of stop-bands has a quasiperiodic resonant character. In the absence of resonance conditions, an (*hkl*) stop-band can be selectively switched by tuning the permittivity of the structural components, whereas at the resonance, a photonic stop-band cannot be switched off by changing the permittivity. A proper choice of the structural and dielectric parameters can create a resonance photonic band determining the Bragg wavelengths, to which a photonic crystal can never be transparent. The theoretical results were experimentally tested on classical photonic crystals, opals. Selective switching of stop-bands was studied by immersion-resolved and polarization-resolved spectroscopy. We found that opals possess all predictable properties of multi-component structures due to inhomogeneity of the constituent a-SiO_2 spheres.

DOI: 10.1103/PhysRevB.77.205106 PACS number(s): 42.70.Qs, 42.25.Fx, 42.79.Fm

I. INTRODUCTION

Over the past two decades, the progress in fundamental and applied studies of photonic crystals (PhCs) has been so remarkable that there is little doubt that PhCs will become basic structures for technologies in the coming age of optoelectronics and telecommunications. The first light-manipulating devices that employ photonic crystals as waveguides to transport light, resonant cavities to trap light, and mirrors to reduce spontaneous emission have already been designed.[1–5]

The unique properties of PhCs are defined by Bragg light diffraction on various (*hkl*) crystal planes, which appears when the lattice constant and the light wavelength match, producing the so-called one-dimensional photonic stop-bands in certain directions[6,7] of the light wave vector **K**. We will call the stop-band resulting from the diffraction on the (*hkl*) plane as the (*hkl*) band. References 8–10 demonstrated that at a certain crystal symmetry and a bulk material to air permittivity ratio, the formation of a completely three-dimensional (3D) photonic band gap is possible. In this case, the propagation of light of a specific frequency range becomes forbidden for all wave vectors **K** within the crystal. Therefore, the dielectric contrast, i.e., the permittivity distribution law through the unit cell, is a key factor that determines the opening of the stop-bands, their energy gap width, and the formation of a complete band gap.

In the current paper, we performed theoretical and experimental investigation of the principles of the selective switching of stop-bands in PhCs. We introduce the following classification of PhCs: crystals consisting of two components with homogeneous permittivity of each component will be referred to as *two-component PhCs*, while we merge all other PhCs into a global term, i.e., *multi-component PhCs*. Such classification appears justified because all the multi-component PhCs exhibit the same abilities to independently switch stop-bands. Among the multi-component PhCs, we will consider two subgroups: (i) *PhCs with an inhomogeneous permittivity profile* $\varepsilon(r)$ and (ii) PhCs with the structure consisting of more than two *homogeneous* components. Below, we will analyze the simplest example of the second subgroup, the *three-component PhCs*, which will permit the description of all the specific properties exhibited by multi-component PhCs. Figure 1 illustrates the classification for one-dimensional, two-dimensional (2D), and 3D PhCs with various numbers of components.

Two-component photonic structures that are studied earlier in detail become fully transparent to light when the permittivity of one component matches that of the other. Thus, two-component PhCs do not permit selective manipulation of propagating light with different Bragg wavelengths. This simplifies the manipulation in two-component PhCs but essentially reduces their functional capabilities and applications since the dielectric contrast does not represent an independent degree of freedom in on/off switching of different (*hkl*) bands.

Therefore, it is very important to design novel PhCs that do not have this limitation. To manipulate light, one should have information about the general mechanisms of on/off switching of single (*hkl*) stop-bands and the overall photonic band structure. One possible way of extending the operational capabilities of PhCs is to make their band structure more complex by employing multi-component PhCs that

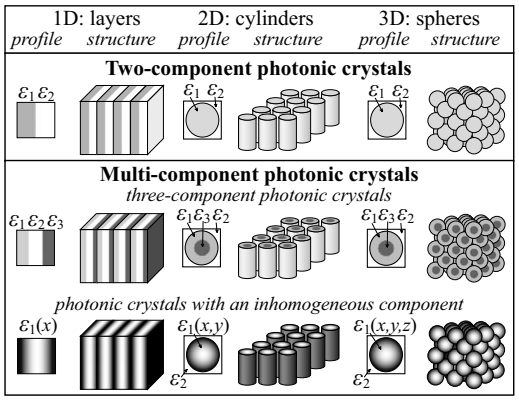

FIG. 1. Simple examples of two- and multi-component photonic crystals for one, two, and three dimensions. The table describes nine structures. The permittivity profile is shown for each of them. The first row contains two-component PhCs, the second one, three-component PhCs, and the third one, PhCs with an inhomogeneous component.

possess a more complex space-periodic dependence of the permittivity modulation. Surprisingly, no systematic attempts have been made so far to understand the photonic behavior of multi-component PhCs. We can mention only four publications: Ref. 11, in which the photonic band structure was calculated along the directions $\Gamma \rightarrow L$ and $\Gamma \rightarrow X$ in coated opals, Ref. 12 an experimental study on coated opals, and Refs. 9 and 13.

In a recent letter,[14] we reported novel properties of Bragg light diffraction in multi-component periodic structures. In contrast to two-component structures, the Bragg diffraction there was found to possess some radically new characteristics that were considered in terms of their application to PhCs. In both Ref. 14 and the present paper, we discuss only photonic band gap systems where the permittivity of only one component is varied while the others remain constant, which is relatively easy to technologically achieve. Employing a different analytical approach to the Bragg diffraction, we found that multi-component PhCs exhibit a quasiperiodic resonance behavior. With resonance, the disappearance of specific (*hkl*) photonic stop-bands is impossible at any permittivity of the variable component. In the absence of resonance, one can perform a selective on/off switching of a specific (*hkl*) stop-band by tuning the permittivity or the structural parameters. Our conclusions were supported by the comparison of the calculations and the spectroscopic data obtained in experiments on synthetic opals.

Note that synthetic opals have long been regarded as very convenient objects to test various theoretical models. It would be appropriate to recall here that opals are made up of a-SiO_2 (silica) spheres of several hundred nanometers in diameter, which are arranged in a close-packed lattice. In natural opals, the interstices are generally filled with amorphous silica mixed with other minerals.[15,16] Today, synthetic opals are fabricated by using commercial technologies.[17,18] They represent samples of ~ 1 cm^3 in size, and most well ordered opals have a face-centered cubic (fcc) lattice.[19] Synthetic opals have voids between a-SiO_2 spheres, which could be filled by liquid or solid fillers with controlled permittivity values.[12,20–26] After the opals were found to be 3D PhCs in the visible spectral region[20,21] and inverted opals were synthesized[27–29] with a complete photonic band predicted in Refs. 9 and 10, the intensive work on PhCs[12,20–26,30,31] promoted active interest in their optical properties. The photonic band structure of synthetic opals, i.e., the wave vector dependence of the stop-band energy in all high-symmetry directions on the Brillouin zone (BZ), was first experimentally investigated in Refs. 24 and 32. Opals also served as the experimental material to study 3D light diffraction underlying the formation of photonic stop-bands.[24,33]

Light scattering in opals was commonly described as the Bragg diffraction from a two-component fcc structure composed of homogeneous a-SiO_2 spheres and a filler.[10] In this case, all the (*hkl*) stop-bands must simultaneously disappear when the permittivity of the spheres matches that of the filler. We have found, however, that the {111}, {200}, and {220} families of stop-bands show different behaviors, depending on the permittivity of the filler, i.e., the variable component,[14] a fact that is inconsistent with the two-component model. Therefore, the permittivity profile of silica spheres plays a crucial role in defining the photonic band structure of opals.

In addition to the results on selective manipulation of photonic stop-bands by varying the filler permittivity,[14] we should mention the studies demonstrating a strong polarization dependence of the Bragg diffraction and transmission spectra of opals.[25,26] Transmission and diffraction experiments have shown that stop-bands disappear in p-polarized light incident onto the (*hkl*) crystal planes at a quasi-Brewster angle θ^{qB}. The strong polarization dependence of the stop-bands can be interpreted within the quasi-Brewster model.[26] It can provide another way to perform selective manipulation of the (*hkl*) bands.

The major goal of the present work was to theoretically and experimentally study the mechanism underlying the switching of photonic stop-bands in multi-component PhCs. We have shown that such PhCs allow a selective on/off switching of a definite (*hkl*) band by varying (modulating) the crystal parameters or by changing the light polarization to provide *a simultaneous control of the information transmitted at different light frequencies*. To theoretically solve this problem, we employed the analytical approach developed in Ref. 14 and present here a detailed description of the method to calculate the structure of PhCs with prescribed parameters of stop-bands. We show that a proper choice of structural and dielectric characteristics can always yield a stop-band that cannot be switched off by changing the permittivity of the variable component. This kind of photonic stop-band will be termed *a resonance band*. The experiments were aimed at obtaining the immersion, polarization, and dispersion dependences of stop-bands from the transmission spectra of white light propagating through oriented preselected samples of high quality synthetic opals. Of special interest were the (*hkl*) bands with high Miller indices, which recently have been examined.[19]

The paper is organized as follows. Section II discusses the analytical approach and the calculation of the nondiffraction regime for different (*hkl*) stop-bands in two- and multi-component PhCs. In Sec. III, we briefly describe the crystal

structure of synthetic opals and the parameters of the experimental samples. Section IV describes the details of the experimental techniques. In addition, we present the calculations of the photonic band structure of opals made in the Bragg approximation, namely, the gap energy $E(\mathbf{K})$ versus the light wave vector $\mathbf{K}$ passing through all high-symmetry points on the Brillouin zone (BZ). Section V presents the experimental data on the photonic band structure with a detailed discussion of the immersion spectroscopic data on single (hkl) stop-bands to show the possibility to manipulate the stop-bands by varying the dielectric contrast to perform on/off switching of separate (hkl) stop-bands. Possible applications of these effects are discussed in Sec. VI, and the main conclusions are summed up in Sec. VII.

II. THEORETICAL BACKGROUND

The principal property of PhCs is the existence of frequency (energy) stop-bands forbidding the propagation of electromagnetic waves through the structure. The condition for a stop-band to arise is the presence of a periodically modulated permittivity $\varepsilon(\mathbf{r})$ or the permittivity contrast $\Delta\varepsilon$.[3–5] In a two-component structure, the stop-band width $\Delta\omega$ is related to the contrast as $\Delta\omega=(2/\pi)\omega\sqrt{\Delta\varepsilon/\varepsilon}$ (Refs. 1 and 34); hence, the condition for the stop-band disappearance is fulfilled when the permittivity of one component matches that of another, $\Delta\varepsilon=0$. If we neglect the possible difference in the dispersion dependences $\varepsilon(\lambda)$ of the materials composing the crystal, this condition will become independent of the energy, the wave vector $\mathbf{K}$, and the (hkl) family of planes that form the stop-bands. In a multicomponent PhC, however, the conditions for the appearance and/or disappearance of stop-bands (the on/off-switching conditions) are more complicated.

Consider a 3D PhC with the fcc structure consisting of nonoverlapping spheres with a spherically symmetrical arbitrary profile of the permittivity $\varepsilon_s(r)$, the intersphere spaces being filled with a homogeneous material having the permittivity ε_f, it is a variable component in our case. If the spheres form a close-packed structure with a point contact between them, their radius normalized to a constant distance between the sphere centers is $r_s=0.5$. Note that at $r_s<0.5$, we deal with a structure consisting of noncontacting spheres fixed by the filler at the fcc-lattice sites. The inverse permittivity of a Wigner–Seitz cell of the crystal is defined as

$$\frac{1}{\varepsilon(r)}=\frac{1}{\varepsilon_f}+\left[\frac{1}{\varepsilon_s(r)}-\frac{1}{\varepsilon_f}\right]\Theta(r_s-r), \tag{1}$$

where $\Theta(x)$ is the unit step function: $\Theta(x)=1$ at $x\geq 0$ and $\Theta(x)=0$ at $x<0$.

We will make use of this generic example because many classes of PhCs such as opals, opal-like polymers, and inverted opals have a lattice quite similar to a perfect fcc lattice.[12,19,21,30] The obtained conclusions can be easily generalized to many other structures. Note that the simple fcc structure is capable to demonstrate many important features of multi-component PhCs: the resonance behavior of photonic stop-bands, the possibility to switch off some $\{hkl\}$ bands by varying the filler permittivity and the failure to do so with other stop-bands, and many other interesting properties. The effect of the disappearance of a dip in the transmission spectra, linked to the variations of the filler permittivity, will be called as "immersion disappearance effect" and the corresponding dependences as "immersion dependences." These photonic properties will be considered below in terms of the approach suggested in Ref. 14.

Note that switching off of a selected band is possible even in two-component PhCs when their geometrical parameters (e.g., sphere radius, see Sec. II B) are being manipulated. However, a technologically more feasible way to selectively switch a stop-band is to use the so-called immersion disappearance effect, the main properties of which appear only in multi-component PhCs. The simplicity of three-component PhCs' structure allows an analytical solution for all the main dependencies of multi-component PhCs' optical properties (see Sec. II C). The more general case of multi-component PhCs with inhomogeneous permittivity profile $\varepsilon(r)$ does not allow such a simple analysis, and the immersion disappearance effect in these PhCs could often be revealed only by using numerical methods (see Ref. 14 and Sec. V C).

A. General approach

To analyze the photonic properties of multi-component PhCs, let us consider the Fourier coefficient of the inverse of the permittivity, i.e., *the scattering form factor* $S(\mathbf{G}_{hkl})$, as follows:

$$S(\mathbf{G}_{hkl})=\frac{1}{V_0}\int_{V_0} d\mathbf{r}\frac{1}{\varepsilon(r)}\exp(-i\mathbf{G}_{hkl}\cdot\mathbf{r}), \tag{2}$$

which describes the intensity of Bragg diffraction from a family of (hkl) crystal planes as a function of the reciprocal lattice vector $\mathbf{G}_{hkl}=h\mathbf{b}_1+k\mathbf{b}_2+l\mathbf{b}_3$, which uniquely determine the direction in the crystal and corresponding $\{hkl\}$ family of planes, where $\{\mathbf{b}_i;i=1,2,3\}$ are the elementary reciprocal lattice vectors and V_0 is the volume of a PhC Wigner–Seitz cell.

The term *the nondiffraction regime* will be further applied to the $\{hkl\}$ planes in the case of the vanishing a scattering form factor $S(\mathbf{G}_{hkl})=0$ when a wave of the Bragg wavelength λ_{hkl} passes through the crystal without being scattered by these planes. Note that electromagnetic radiation in a PhC could be described by using Bloch waves of a given frequency but not of a given wavelength. Therefore, under the term "wavelength" in this paper, we imply the value corresponding to the propagation of the waves in vacuum. If the inverse permittivity $1/\varepsilon(r)$ is described by Eq. (1), the condition $S(\mathbf{G}_{hkl})=0$ at $\mathbf{G}=0$ is

$$S(0)=\frac{1-f}{\varepsilon_f}+\frac{1}{V_0}\int_{V_0} d\mathbf{r}\frac{1}{\varepsilon_s(r)}\Theta(r_s-r)=0, \tag{3}$$

where $f=4\pi r_s^3/3V_0$ is the volume fraction of a sphere: $V_0=a_{oo}^3/\sqrt{2}$, where a_{oo} is the distance between the sphere centers in the fcc lattice. Note that we have $f=\pi\sqrt{2}/6\approx 0.74$ for the case of a point contact of close-packed spheres at $a_{oo}=2r_s$.

At $|\mathbf{G}_{hkl}|\neq 0$, the relation $S(\mathbf{G}_{hkl})=0$, to be discussed below in detail, is rewritten as

$$S(\mathbf{G}_{hkl}) = \frac{1}{V_0}\int_{V_0} d\mathbf{r}\left[\frac{1}{\varepsilon_s(r)} - \frac{1}{\varepsilon_f}\right]\Theta(r_s - r)\exp(-i\mathbf{G}_{hkl}\cdot\mathbf{r}) = 0. \tag{4}$$

By integrating over the angular variables of the spherical coordinates in Eq. (4), we can find the filler permittivity $\varepsilon_f^0(G_{hkl})$ that meets the condition of the zero scattering form factor as follows:

$$\varepsilon_f^0(G_{hkl}) = \frac{\frac{1}{G_{hkl}^2}[\sin(G_{hkl}r_s) - G_{hkl}r_s\cos(G_{hkl}r_s)]}{\int_0^{r_s}\frac{r}{\varepsilon_s(r)}\sin(G_{hkl}r)dr}$$

$$= \frac{\frac{1}{G_{hkl}^2}R(G_{hkl}, r_s)}{\int_0^{r_s}\frac{r}{\varepsilon_s(r)}\sin(G_{hkl}r)dr}. \tag{5}$$

Here, we have designated the Rayleigh–Hans function as $R(G,r)=\sin(Gr)-Gr\cos(Gr)$.

To understand the behavior of $\varepsilon_f^0(G_{hkl})$ as a function of the reciprocal lattice vector $\mathbf{G}_{hkl}$, we do not limit it to the discrete values G_{hkl} but rather consider it as a continuous function G and omit the hkl indices. Note that the values of $G_{hkl}=\pi\sqrt{2(h^2+k^2+l^2)}a_{oo}^{-1}$ for the $\{hkl\}$ planes experimentally studied in this work are $G_{111}=7.695$, $G_{200}=8.886$, $G_{220}=12.566$, $G_{311}=14.735$, and $G_{222}=2G_{111}=15.390$ (here and below, the values of G_{hkl} are taken in the units of the reciprocal distance between the sphere centers a_{oo}^{-1}).

It is also important to note that one should be careful in using conditions (4) and (5) in the case of a multiple Bragg diffraction regime, i.e., when stop-bands corresponding to different $\mathbf{G}_{hkl}$ overlap. In this case, nondiffraction condition should be obtained by solving the full eigenvalue problem using numerical methods such as the plane wave expansion[8–10] and the Korringa-Kohn-Rostocker (KKR).[35]

B. Two-component three-dimensional Crystals: Switching off stop-bands selectively by varying structural parameters

We will first consider a simple case of a two-component 3D photonic crystal (Fig. 1), whose fcc lattice is composed of homogeneous spheres, $\varepsilon_s(r)=\varepsilon_s=$const, immersed in a homogeneous filler ε_f, with the following inverse permittivity:

$$\frac{1}{\varepsilon(r)} = \frac{1}{\varepsilon_f} + \left(\frac{1}{\varepsilon_s} - \frac{1}{\varepsilon_f}\right)\Theta(r_s - r). \tag{6}$$

At $|\mathbf{G}_{hkl}| \neq 0$, the expression for the scattering form factor (4) is

$$S(G) = \frac{4\pi\sqrt{2}}{(Ga_{oo})^3}\left(\frac{1}{\varepsilon_s} - \frac{1}{\varepsilon_f}\right)R(G, r_s). \tag{7}$$

It follows from Eq. (7) that the nondiffraction regime $S(G)=0$ is valid for a two-component PhC in two cases. Only one of them is usually considered in the literature: when the vanishing of the form factor is defined by the vanishing of the first bracketed term in Eq. (7), i.e., when the matching condition for the permittivity $\varepsilon_f^0=\varepsilon_s$ is reached [we get a similar relation after the integration of the denominator in Eq. (5) with $\varepsilon_s(r)=\varepsilon_s=$const]. Obviously, when the medium becomes optically homogeneous, the matching condition $\varepsilon_f^0=\varepsilon_s$ is the condition for *a simultaneous disappearance of all the* $\{hkl\}$ stop-bands.

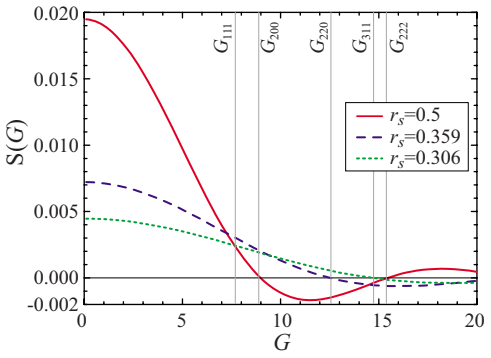

FIG. 2. (Color online) The scattering form factor $S(G)$ for the two-component fcc lattice with the sphere radii $r_s=0.5$ (point contact), $r_s=0.359$ (the nondiffraction regime for the {220} planes), and $r_s=0.306$ (the nondiffraction regime for the {311} planes) calculated from formula (7) at $\varepsilon_s=1.9$ and $\varepsilon_f=2.0$. The moduli of the shortest reciprocal lattice vector G_{hkl} are shown by vertical lines.

In addition to this trivial case, the nondiffraction regime may occur when the Rayleigh–Hans function $R(G,r_s)$ vanishes. The $S(G)$ function for a two-component PhC, described by Eq. (7) with the parameters $\varepsilon_s=1.9$ and $\varepsilon_f=2.0$, is shown in Fig. 2, which also gives the module values of the reciprocal lattice vector G for the $\{hkl\}$ family of planes with the lowest Miller indices. The zeros in the Rayleigh–Hans function are defined as

$$\tan Gr_s = Gr_s. \tag{8}$$

If the solution to Eq. (8), i.e., G_i, coincides with one of the parameters G_{hkl}, the scattering form factor (7) will turn to zero for the $\{hkl\}$ family of planes. In the fcc lattice made up of regular close-packed spheres with a point contact ($r_s=0.5$), the first root G_1 in Eq. (8) is close to the value of $G_{200}=8.886$ (Fig. 2). However, if we consider a hypothetical structure made up of noncontacting spheres fixed by a filler at the lattice sites, we get $G_1=G_{220}$ when the sphere radius is as small as $r_s=0.359$, which means that the nondiffraction regime for the {220} planes is fulfilled. If the sphere radius is made still smaller, we have the condition $G_1=G_{hkl}$ for the higher index planes (Fig. 2). It can be concluded from this analysis that the diffraction cannot be switched off in the (111) plane of a two-component structure. Besides, the condition $G_i=G_{hkl}$ is defined only by the parameter r_s and is independent of ε_s or ε_f. By varying the sphere size, therefore, we can create two-component PhCs with a selected (hkl) stop-band switched off. On the other hand, the modulation of the permittivity does not provide on/off switching of a desired (hkl) stop-band.

C. Three-component three-dimensional crystals (coated spheres): Switching off stop-bands selectively by varying structural and dielectric parameters

Consider a practically feasible three-component 3D PhC (Fig. 1). Suppose that the fcc structure is formed by spheres, each consisting of a homogeneous nucleus of radius r_n with the permittivity ε_n, having a homogeneous coat of ε_c and the outer radius r_c. The intersphere space is assumed to be filled with a homogeneous material with ε_f. Then, the inverse permittivity of a Wigner–Seitz cell is defined as

$$\frac{1}{\varepsilon(r)} = \frac{1}{\varepsilon_f} + \left(\frac{1}{\varepsilon_n} - \frac{1}{\varepsilon_c}\right)\Theta(r_n - r) + \left(\frac{1}{\varepsilon_c} - \frac{1}{\varepsilon_f}\right)\Theta(r_c - r). \tag{9}$$

By substituting Eq. (9) into Eq. (2), we can derive the following condition for the nondiffraction regime at $G \neq 0$:

$$S(G) = \frac{4\pi\sqrt{2}}{(Ga_{oo})^3}\left[\left(\frac{1}{\varepsilon_n} - \frac{1}{\varepsilon_c}\right)R(G,r_n) + \left(\frac{1}{\varepsilon_c} - \frac{1}{\varepsilon_f}\right)R(G,r_c)\right]$$
$$= S_1(G) + S_2(G) = 0. \tag{10}$$

A comparison of Eq. (7) for the scattering form factor of a PhC made up of homogeneous spheres and Eq. (10) leads one to the conclusion that the scattering form factor of a three-component PhC includes two terms: (1) $S_1(G)$ that describes the contribution of the scattering from the homogeneous spheres with the permittivity ε_n and the radius r_n, having a homogeneous coat ε_c, and (2) $S_2(G)$ that defines the contribution of the scattering from the homogeneous spheres with the permittivity ε_c and radius r_c, immersed in a filler with ε_f. Both terms are alternating in sign and depend on the permittivity ratio and the sign of the respective Rayleigh–Hans function $R(G,r_s)$. To illustrate, consider the fcc opal structure with a variable filler permittivity, and the quantity to be defined is the function $\varepsilon_f^0(G)$. Formula (10) yields the expression for the nondiffraction regime in a three-component PhC,

$$\frac{1}{\varepsilon_f^0(G)} = \frac{1}{\varepsilon_c} + \left(\frac{1}{\varepsilon_n} - \frac{1}{\varepsilon_c}\right)\frac{R(G,r_n)}{R(G,r_c)}, \tag{11}$$

It follows from expressions [Eq. (11)] that ε_f^0 vary with G and with all the parameters of the structure: ε_n, ε_c, r_n, and r_c. This means that we get different conditions of the nondiffraction regime for different $\{hkl\}$ photonic bands. In other words, there is a possibility of on/off switching of a definite (hkl) stop-band by modulating the dielectric permittivity of one of the components.

Let us now discuss an opal structure with the nucleus of radius r_n=0.4 composed of a-SiO_2 material with permittivity of ε_n=1.9 [21,36] with different coats (r_c=0.5, point contact of the spheres) and a permittivity smaller than (ε_c=1.0), equal to (ε_c=1.9), and larger than (ε_c=5,11) that of the nucleus (Fig. 3). At $\varepsilon_n=\varepsilon_c$, the quantity ε_f^0 corresponding to the nondiffraction regime is seen to be independent of G, so the structure becomes fully transparent when the filler permittivity matches the permittivities of the nucleus and the coat,

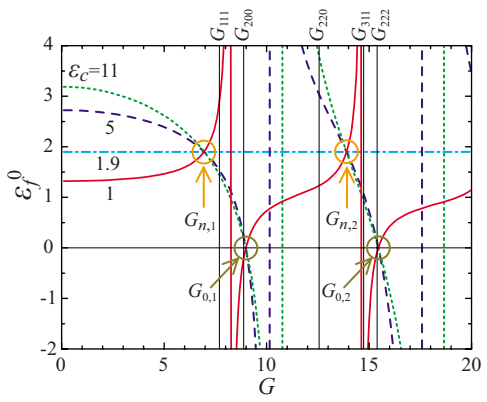

FIG. 3. (Color online) The filler permittivity $\varepsilon_f^0(G)$ of a three-component photonic crystal in the nondiffraction regime as a function of the reciprocal lattice vector G calculated from Eq. (11) for a fcc structure composed of close-packed spheres with the nucleus of radius r_n=0.4(ε_n=1.9) and different coats (r_c=0.5, ε_c=1.0, 1.9, 5, 11). The moduli of the shortest reciprocal lattice vector G_{hkl} are shown by vertical lines.

$\varepsilon_f^0=\varepsilon_n=\varepsilon_c$=1.9 (the cyan dash-dot line in Fig. 3). At $\varepsilon_n \neq \varepsilon_c$, the $\varepsilon_f^0(G)$ function shows a complex resonance behavior possessing the following features.

(i) The $\varepsilon_f^0(G)$ functions show a quasiperiodic behavior with the resonance features at $G=G_{\text{res}}$. The resonance values are found from the following relation:

$$\left(\frac{1}{\varepsilon_n} - \frac{1}{\varepsilon_c}\right)R(G,r_n) + \frac{1}{\varepsilon_c}R(G,r_c) = 0, \tag{12}$$

which is derived from Eq. (10) at $\varepsilon_f \to \pm\infty$. It follows from Eq. (12) that the resonance values of G_{res} are determined by both the dielectric parameters ε_n and ε_c and by the structural parameters r_n and r_c. For example, in a fcc structure made up of a-SiO_2 spheres (r_n=0.4, ε_n=1.9) coated with silicon (r_c=0.5, ε_c=11), the first two resonances $\varepsilon_f^0(G)$ correspond to $G_{\text{res}} \approx 10.8$ and 18.7 (the vertical green dotted lines in Fig. 3). The Bragg diffraction from the resonance $\{hkl\}$ planes meeting the requirement $G_{hkl}=G_{\text{res}}$ will always take place and cannot be switched off by changing the filler permittivity.

It is noteworthy that *the resonance condition* $G_{hkl}=G_{\text{res}}$ *can always be accomplished by appropriately choosing the parameters of the multi-component structure*. For example, the resonance condition $G_{hkl}=G_{\text{res}}$ in Eq. (12) for a three-component fcc structure can be regarded as the G_{res} dependence on the variable parameters ε_c, ε_n, and r_n. If we take ε_c as a single variable, Eq. (12) will yield the coat permittivity values at which an $\{hkl\}$ photonic band becomes resonant ($G_{hkl}=G_{\text{res}}$),

$$\varepsilon_c(\text{res}_{hkl}) = \varepsilon_n\left[1 - \frac{R(G_{hkl},r_c)}{R(G_{hkl},r_n)}\right]. \tag{13}$$

For instance, to make the {220} band family (G_{220}=12.566) resonant in a fcc structure composed of close-packed coated spheres (with the parameters ε_n=1.9, r_n=0.4, and r_c=0.5), one should take the coat permittivity to be

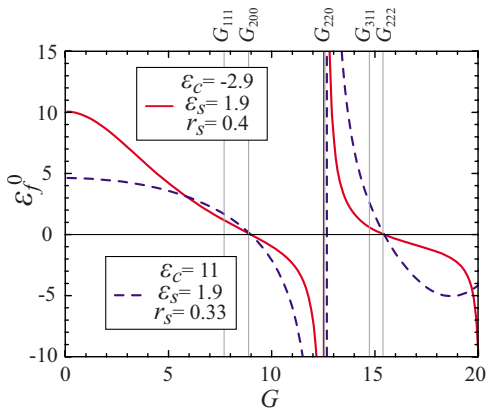

FIG. 4. (Color online) The filler permittivity $\varepsilon_f^0(G)$ in the nondiffraction regime as a function of the reciprocal lattice vector G calculated from Eq. (5) for a fcc structure composed of close-packed spheres with the nucleus r_n=0.33,ε_n=1.9 and a coat r_c =0.5, ε_c=11 (the blue dashed curve) and of spheres with the nucleus r_n=0.4, ε_n=1.9 and a coat r_c=0.5, ε_c=−2.87 (the red solid curve). The moduli of the shortest reciprocal lattice vector G_{hkl} are shown by vertical lines. The first resonance G_{res} for both $\varepsilon_f^0(G)$ functions matches G_{220}=12.566.

$\varepsilon_c(\text{res}_{220})$=−2.87 (Fig. 4). In order to calculate a structure consisting of preselected compounds, the variable parameter should be the nucleus of radius r_n. To illustrate for a a-SiO_2 fcc structure (ε_n=1.9) coated with silicon (ε_c=11), the numerical solution of Eq. (12) with respect to r_n will give the following value determining the resonance for the {220} photonic bands: $r_n(\text{res}_{220})$=0.33 (Fig. 4).

(ii) An important feature of the $\varepsilon_f^0(G)$ function is the presence of quasiperiodic points at G=G_0, where we have $\varepsilon_f^0(G_0)\equiv 0$ irrespective of the values of ε_c or ε_n, except for the case of ε_f^0=ε_c=ε_n (the cyan dash-dot line in Fig. 3). This feature arises when the function $R(G,r_c)$ in the second term $S_2(G)$ of Eq. (10) becomes zero. In this case, the nondiffraction regime $S_1(G)+S_2(G)=0$ with the first nonzero term, $S_1(G)\neq 0$, can be obtained at $\varepsilon_f^0\to 0$ only when the second term contains an uncertainty with the finite value equal to $-S_1(G)$. The G_0 values are found from the following relation:

$$\tan Gr_c = Gr_c, \tag{14}$$

and they do not depend on the parameters ε_c, ε_n, or r_n. At r_c=0.5, the two minimum values of G_0 are ≈9.0 and 15.5 (Fig. 3).

(iii) Another specific feature of the $\varepsilon_f^0(G)$ function is the presence of special quasiperiodic points at G=G_n when ε_f^0 does not vary with ε_c. The G_n values are found from the following equation:

$$R(G,r_n) = R(G,r_c). \tag{15}$$

At r_n=0.4 and r_c=0.5, the two minimum values of G_n are ≈7.0 and 13.9 (Fig. 3). At these special G_n points, the conditions for the nondiffraction regime change. Consider, as an illustration the range of the minimum G values (before the first resonance G_{res}). In the range of $G<G_n$ at $\varepsilon_n<\varepsilon_c$, we have the relation $\varepsilon_n<\varepsilon_f^0<\varepsilon_c$, while at $\varepsilon_n>\varepsilon_c$, there is the opposite relation, $\varepsilon_n>\varepsilon_f^0>\varepsilon_c$. Therefore, for the scattering to be compensated and for the nondiffraction regime to be accomplished at $G<G_n$, the filler permittivity must differ from the nucleus permittivity by the same value as the coat permittivity, i.e., the optical densities of both media must be simultaneously higher or lower than the nucleus density. The opposite condition is fulfilled at larger G values after the special point G_n, in the range $G_n<G<G_{\text{res}}$. The higher optical density of the coat, $\varepsilon_n<\varepsilon_c$, is compensated by the lower density of the filler, $\varepsilon_n>\varepsilon_f^0$, and vice versa: the lower coat density, $\varepsilon_n>\varepsilon_c$, is compensated by the higher filler density, $\varepsilon_n>\varepsilon_f^0$. For instance, the nondiffraction regime at ε_c =1.0, ε_n=1.9, and G=G_{111}≈7.7 is achieved at $\varepsilon_f^0\approx 2.9(\varepsilon_f^0>\varepsilon_n>\varepsilon_c)$, whereas at ε_c=11, it occurs at $\varepsilon_f^0\approx 1.4$ $(\varepsilon_f^0<\varepsilon_n<\varepsilon_c)$ (Fig. 3). These conditions, however, again become inverted with further increase in G after the first resonance point ($G_{\text{res}}\approx 8.3$ for ε_c=1.0 and $G_{\text{res}}\approx 10.8$ for ε_c=11) and so on (Fig. 3). This behavior is determined by the periodic nature of the functions defining the nondiffraction regime in Eq. (10).

Similarly, we can consider the opal structure, whose nondiffraction regime is provided by varying the nucleus permittivity $\varepsilon_n^0(G)$ and the coat permittivity $\varepsilon_c^0(G)$, as in the case of so-called inverted opals.[27–29]

Thus, the presence of inhomogeneities in a multicomponent PhC leads to a G-dependent variation in ε_f^0. Generally, this allows a selective manipulation of the (hkl) photonic stop-bands.

Additionally, we can consider requirements for the nondiffraction regime depending on the structural parameters, similar to what was already described in the Sec. II B for the two-component PhCs.

III. OPAL STRUCTURE AND SAMPLE CHARACTERIZATION

Opals are 3D photonic crystals consisting of uniformly sized close-packed a-SiO_2 (silica) spheres that are commonly postannealed at a high temperature to sinter. During annealing, the silica spheres demonstrate pronounced changes in the dielectric constant,[37] which can be linked to the changes in the structure of the spheres. A complete densification of spheres does not take place even at 600 °C and their refractive index is consistently lower than that of fused quartz. Interestingly, the value of the refractive index as a function of annealing temperature shows a minimum at intermediate temperatures, which can be interpreted as being due to the initial removal of material from pores in the spheres at lower temperatures and to a slow elimination of pores at higher temperatures.[37] Transmission electron microscopy (TEM) has confirmed the lack of homogeneity and the presence of pores within opal spheres.[14] As the structure of spheres may strongly depend on the synthesis conditions, we performed an independent TEM and scanning electron microscopy (SEM) analysis on all the opals used in our study.

The microstructure of silica spheres was investigated by using high-resolution TEM. The TEM samples were prepared by crushing opals in a rubber coated mortar, followed by a 5 min sonication of the powder in isopropanol with a

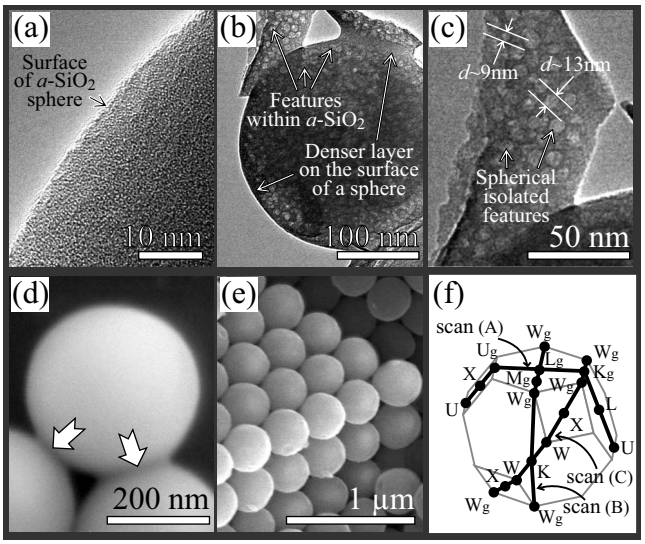

FIG. 5. [(a)–(c)] Transmission and [(d)–(e)] scanning electron micrographs of opal samples. The fcc close-packed silica spheres show a smooth dense surface and a porous interior. The Brillouin zone of the fcc lattice is a truncated octahedron centered at Γ (f).

subsequent deposition on a lacey-carbon coated copper grid (200 mesh). A field-emission TEM microscope (JEOL 2010F, Japan) with an imaging filter (Gatan GIF) was used at 200 kV. The SEM study was performed by using an FEI XL30 environmental field-emission electron microscope (Netherlands) operating at an accelerating voltage of 10 kV. The samples were uncoated and were studied at a working distance of 5–8 mm. The chamber pressure of 1 Torr allowed minimization of the surface charging.

High-resolution TEM of the spheres revealed their smooth surface and amorphous microstructure [Fig. 5(a)]. The absence of nanocrystals was also confirmed by electron diffraction data (not shown). Lower resolution micrographs [Figs. 5(b) and 5(c)] were recorded at a strong defocusing to provide clear imaging of the compositional discontinuities through the appearance of Fresnel fringes and enhanced contrast. Pores in the silica spheres were observed in all the samples, supporting the results of the previous studies.[38] They appear as lighter areas in the micrographs [Figs. 5(b) and 5(c)] due to the smaller projected potential and, hence, the weaker scattering of electrons as they travel through the pore-containing silica layer. Due to the spherical shape of the particles and the relatively large sphere diameter (310–340 nm), clear observations of the pore sizes and shapes were only possible in thinner silica fragments [Fig. 5(c)]. Most of the pores are spherical, 7–15 nm in diameter, and isolated from each other [Fig. 5(c)]. The sphere-to-sphere contact area marked by thick white arrows in the micrographs as well as the 10–30 nm near-surface region do not contain pores and are therefore expected to have a higher average density. This variation in the optical density across the spheres indicates a multi-component nature of as-produced synthetic opals.

SEM data confirmed the smoothness of the silica surface [Figs. 5(d) and 5(e)] and demonstrated a high degree of ordering within the close-packed layers of the silica spheres (not shown). Bulk opal samples are formed via consecutive superposition of the (111) layers along the [111] axis (in the designations of the fcc lattice). The close packing of layers can produce, in addition to the fcc lattice, other high density structures, which are both well ordered, e.g., the hexagonal close-packed (hcp) lattice, and variously disordered, e.g., the twin fcc lattice.[24,33] The intersphere spaces can be filled with liquid or solid materials, allowing variation in the opal-filler dielectric contrast and, hence, modification of photonic stop-bands. We will denote the [111] growth direction as $\Gamma \rightarrow L_g$, in contrast to the three other equivalent nongrowth directions $\Gamma \rightarrow L$ in a fcc lattice [Fig. 5(f)]. Besides, the high symmetry points on the BZ surface that belong to the same hexagonal plane as the L_g point will also be marked with the subscript g.

In this work, we studied high quality samples predominantly with the fcc lattice that were investigated earlier.[14,39] All of the samples were cut out of a large bulk sample, whose spherical a-SiO_2 particles had the diameter $D = 315 \pm 15$ nm, as shown by the SEM and optical spectroscopic data.[39] Most of the experimental data presented below were obtained from a rectangular parallelepiped sample, in which two sides of $\sim 7.2 \times 3.0$ mm^2 formed a plane coinciding with the (111) growth plane, while the third plane (~ 0.6 mm) normal to it was oriented along the [111] growth axis. The average sphere size found from the comparison of the experimental data and calculations (Sec. V C) was $D \sim 317$ nm.

IV. EXPERIMENTAL TECHNIQUES

The most suitable way to detect any modification in different (hkl) stop-bands from the variation in the dielectric contrast is to use transmission spectroscopy.[24]

A. Experimental setup

Transmission spectra from synthetic opals were taken during direct passage of white linearly polarized (using a Glan-Taylor prism) light through an oriented sample by employing a two-beam Perkin Elmer Lambda-650 spectrophotometer in the wavelength range of 215–850 nm. The sample was placed at the center of a vessel with plane-parallel quartz windows, which was filled with an immersion liquid. The liquid served as the opal filler and as the ambient medium for the sample. We used two liquids—distilled water with $\varepsilon_w = 1.78$ and propylene glycol with $\varepsilon_{pg} = 2.05$, as well as their mixtures providing the variation in the dielectric constant of the filler in the range of $1.78 \leq \varepsilon_f \leq 2.05$. The permittivities of the liquids were measured by an Abbe IRF-454B2M refractometer. The fillers were chosen from the following criteria. First, these liquids possess a high optical transparency in a wide spectral range: water allows measurements to be made in the wavelength range of 215–850 nm and propylene glycol in the range of 260–850 nm. Second, among liquids transparent in a wide spectral range, water has the lowest permittivity and propylene glycol has the highest permittivity. Our experiments were performed at a low opal-filler dielectric contrast when light was practically not reflected or

refracted by the sample surface, in which case the effects of the sample shape and surface morphology were negligible.

In order to take spectra at various orientations of the opal fcc-lattice relative to the incident light beam, the sample was rotated around two axes normal to each other and an additional axis by using a movable goniometer. The angular accuracy of the sample orientation relative to the incident beam was 0.5°. The beam cross section on the sample was less than 2 mm^2 with the incident light cone spanning less than 6° from the normal incidence.

We took the following precautions to avoid undesirable effects on the measurements induced by possible structural defects of the opals and/or the filler inhomogeneity: (i) the samples had different sphere diameters, (ii) the {111} stop-bands were investigated at different incidence, (iii) the samples were infiltrated with three liquids possessing different viscosities but the same permittivity, (iv) the samples were kept in an ultrasonic bath, and (v) all the transmission spectra were measured at three time moments: immediately after the infiltration, 24 h later, and a week after the infiltration. The analysis of the experimental data showed that all the results to be reported below were reproducible and were not specific to the sample or the method. Here, we discuss the results obtained for the sample of 317 nm spheres.

B. Calculation of dispersion dependences of photonic stop-bands in a low contrast face-centered cubic lattice

The photonic band structure was experimentally studied by scanning the light wave vector **K** across the BZ surface. In order to obtain complete information on stop-bands in a fcc lattice, it is sufficient to calculate the band structure and to measure the light transmission spectra for three scan planes of the wave vector **K** in the BZ: (A) $\Gamma L_g K_g L$, (B) $\Gamma L_g W_g K$, and (C) $\Gamma K_g W_g X$ planes [Figs. 5(f) and 6(a)–6(c)]. Scan planes (A) and (B) contain the common $\Gamma \rightarrow L_g$ axis (the [111] growth direction) and are normal to each other; the planes (A) and (C) contain the common $\Gamma \rightarrow K_g$ axis and are also normal to each other. In these scans, the wave vector passes through the following special points on the BZ:

$$(\mathrm{A}) X \rightarrow U_g \rightarrow L_g \rightarrow K_g \rightarrow L \quad -55^\circ \leq \theta_A \leq 70^\circ, \tag{16a}$$

$$(\mathrm{B}) L_g \rightarrow W_g \rightarrow K \quad 0 \leq \theta_B \leq 90^\circ, \tag{16b}$$

$$(\mathrm{C}) K_g \rightarrow W_g \rightarrow X \quad 0 \leq \theta_C \leq 45^\circ. \tag{16c}$$

The relations of Eqs. (16a)–(16c) also indicate the variation in the incidence angle θ_i (the wave vector **K**) with respect to the fcc structure for each scan, which agrees well with the experimentally obtained data. The data can be adequately interpreted if we attribute the observable spectral features to the respective (hkl) bands, using different models and calculations. At a low dielectric contrast, the most effective approach is to use the dispersion dependences of the (hkl) bands calculated in a simple Bragg approximation.[19] It is shown that the stop-band dispersion can be described well in the approximation of Bragg diffraction in the (hkl) planes

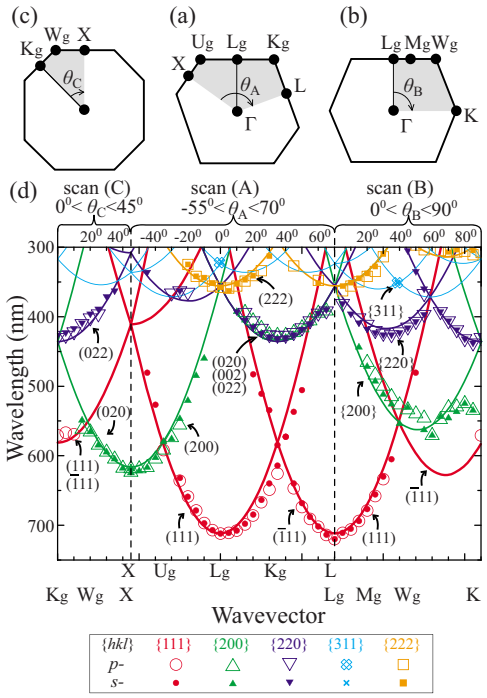

FIG. 6. (Color online) Three cross sections of the Brillouin zone of the fcc lattice made by the scanning planes (a) A, (b) B, and (c) C. (d) Symbols are the measured positions of the dip minima in the transmission spectra for the three paths at the angles θ_i along the upper abscissa. The symmetry points along the paths are shown in the lower abscissa. The solid curves are calculations from Eq. (18) for the filler with $c\ \varepsilon_f = 1.78$ (water).

of a fcc lattice. The dependence of the Bragg wavelength $\lambda_{(hkl)}$ in vacuum on the angle θ_{hkl} of the light incidence onto the (hkl) planes can be found from the following expression:

$$\lambda_{(hkl)}(\theta) = 2d_{111}\sqrt{\varepsilon_{\mathrm{av}}}\left(\frac{3}{h^2+k^2+l^2}\right)^{1/2} \cos\,\theta_{(hkl)}, \tag{17}$$

where d_{111} is the distance between the neighboring (111) planes and $\varepsilon_{\mathrm{av}} = 0.74\tilde{\varepsilon}_s + 0.26\varepsilon_f$ is the average dielectric constant of a perfect opal-filler fcc structure with a point contact of close-packed a-SiO_2 spheres. The calculations, to be described in Sec. V C, yield the value of $\tilde{\varepsilon}_s = 1.92$ and, hence, the values of $\varepsilon_{\mathrm{av}}$ for each filler used in the experiment with the known ε_f. The fitting of the experimental $\lambda_{(hkl)}(\theta)$ dependences with formula (17) gives the parameter $d_{111} \sim 259$ nm and the average sphere diameter $D = \sqrt{3/2}d_{111} \sim 317$ nm for the sample used in the experiment.

Figure 6 shows the theoretical dispersion dependences of the Bragg wavelengths $\lambda_{(hkl)}(\theta)$ for scans (A), (B), and (C) in different (hkl) planes of the following plane families experimentally studied: {111} (712 nm), {200} (617 nm), {220} (436 nm), {311} (372 nm), and {222} (356 nm). In the brackets, we give the maximum wavelengths $\lambda_{(hkl)}(0)$ for water-filled opals.

V. RESULTS AND DISCUSSION

A. Photonic band structure of synthetic opals

We would like to start the discussion of the experimental data with a general remark about light transmission spectra

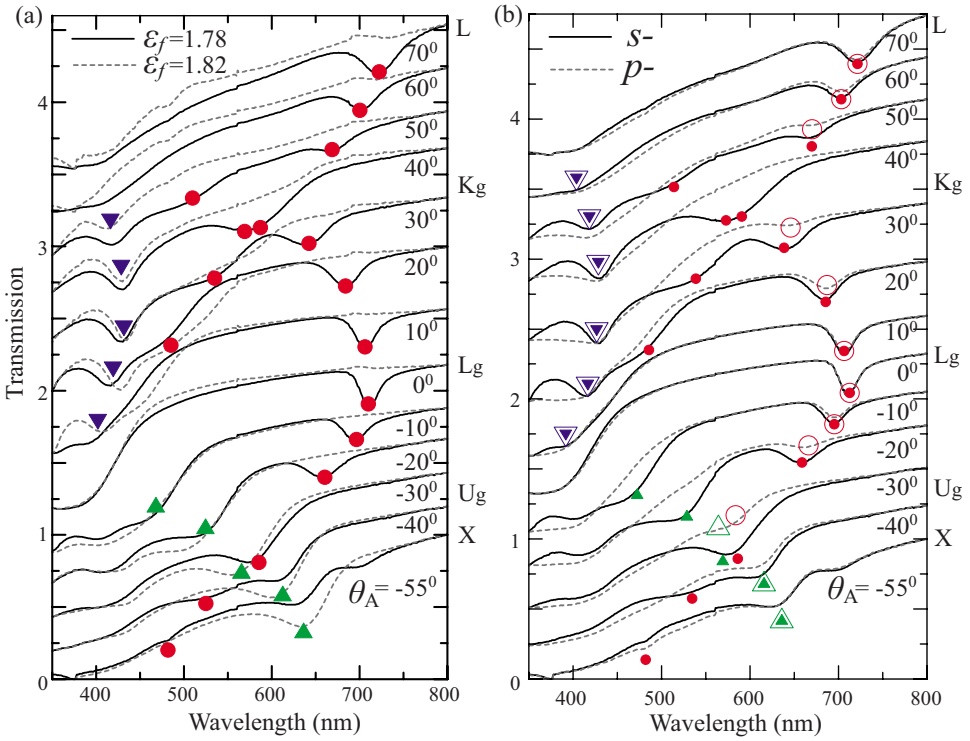

FIG. 7. (Color online) Transmission spectra taken in the whole range of angles $-55° \leq \theta_A \leq 70°$ for scan (A): (a) in s polarization at two permittivity values of the filler, $\varepsilon_f = 1.78$ (solid), 1.82 (dashed); (b) in the s and p polarizations $\varepsilon_f = 1.78$. The solid curve and solid symbols, s polarization; dashed curve and open symbols, p polarization; symbols, experimental minima. The meaning of the symbols is the same as in Fig. 6: red circles, the {111} bands; green triangles, the (200) band; inverted blue triangles, the band defined by the (020), (002), and (022) regions.

of photonic crystals. It is well known that such spectra contain characteristic "opaque" bands directly related to the light diffraction in the definite (hkl) planes, i.e., to the photonic band structure.[24] The actual stop-bands, i.e., bands with nearly zero light transmission through the crystal lattice in a certain direction, may not be experimentally observed for several reasons, including a low contrast of the dielectric permittivities, the finite sample size, and noncollinearity of the light beam. So, we will refer to all bands having a diffraction nature as *photonic bands*.

The transmission spectra were measured in the whole range of incidence angles θ_A, θ_B, and θ_C by scans (A), (B), and (C) in s- and p-polarized light passing through opal samples of 0.6 mm thick filled with different liquids ($1.78 \leq \varepsilon_f \leq 2.05$). Figure 7(a) illustrates the transmission spectra from the (A) scan taken in the s polarization from a water-filled sample ($\varepsilon_f = 1.78$) and a sample filled with a mixture of water and propylene glycol ($\varepsilon_f = 1.82$). The comparison of the data given in Fig. 7(a) and the dispersion dependences calculated from formula (17) enables one to attribute most of the spectral features to the particular (hkl) planes and, hence, to the (hkl) photonic bands. The experimental dependences of the band positions obtained from the spectral processing are presented in Fig. 6. The spectra also contain bands that we failed to attribute. Some of them lie in the short wavelength region containing a large number of intercepting dispersion curves $\lambda_{(hkl)}(\theta)$, which are hard to attribute to a particular (hkl) photonic band. The unattributed bands may also be due to various defects in the fcc lattice.

B. Immersion dependences for the {*hkl*} photonic bands

Our major task in making the experiments was to find the immersion dependences of the various {hkl} photonic band families. In addition to the {111}, {200}, and {220} band families examined in Ref. 14, we studied the immersion for the {311} and {222} photonic bands. We would like to emphasize that in this work, the immersion dependences were first found for the {hkl} bands in all high-symmetry directions on the BZ by making the (A), (B), and (C) scans in both light polarizations, p and s. Below, we discuss the behavior of each {hkl} band family at varying permittivity contrast in the opal-filler system.

1. {111} family, the nondiffraction regime at $\varepsilon_f^0(G_{111}) = 1.82$

The successful identification of these bands is primarily due to the fact that $\lambda_{\{111\}}(0)$ is the longest wavelength in the photonic band spectrum [see formula (17)], defining the red diffraction cutoff in the fcc structure. In our experiments, its value for water-filled opals was found to be $\lambda_{\{111\}}(0) = 712$ nm (the $\Gamma \rightarrow L_g$ path in Figs. 6 and 7).

Figure 7(a) presents the transmission spectra for opals filled with two materials, one of which (water/propylene glycol, $\varepsilon_f = 1.82$) showed the disappearance of the {111} photonic bands. Note the close value of $\varepsilon_f^0(G_{111}) = 1.83$ obtained in Ref. 14. The details of the immersion dependence of a single (111) band are given in Fig. 8(a) for the scattering geometry $\Gamma \rightarrow L_g$ and in Fig. 8(b) for $\Gamma \rightarrow M$. Here, we introduce a new point M on the surface of the Brillouin zone of the fcc lattice in the middle of $L_g - W_g$. This point corresponds to the angle of $\theta_B = 20°$ for scan (B).

Figure 9 presents the results of the spectral analysis showing the normalized square root of the intensity of the dips matching the experimental (hkl) photonic bands as a function of the filler permittivity ε_f. Under the term "dip intensity," we imply intensity of the peak in the extinction spectra $\chi(\lambda) = -\ln T(\lambda)/d$, assuming that the amplitude of the wave,

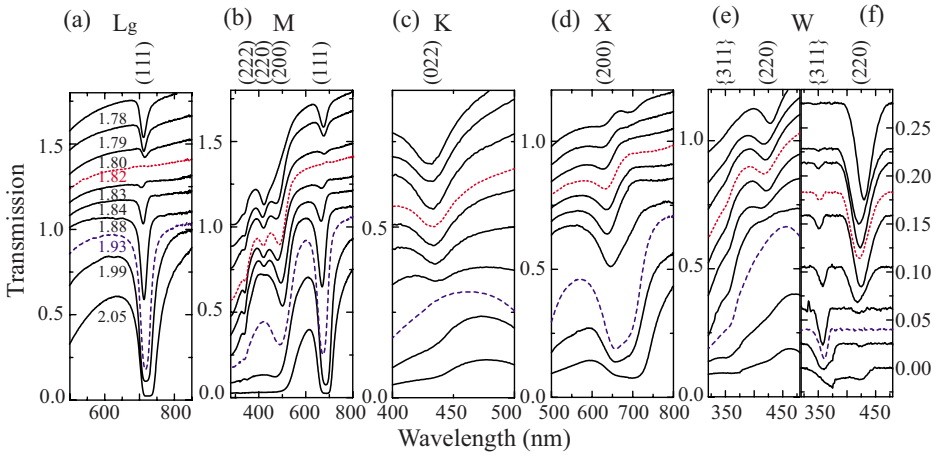

FIG. 8. (Color online) [(a)–(e)] The immersion dependence of the transmission spectra in the whole range of the filler permittivity $1.78 \leq \varepsilon_f \leq 2.05$. The spectral regions and scattering geometries (with special points in the Brillouin zone) indicate the most typical immersion behavior of the photonic band families {111} (L_g, M), {200} (M,X), {220} (M,K,W), {311} (W), and {222} (M). (f) The processed spectra are shown in frame (e). The filler permittivity values ε_f given in frame (a) also refer to the respective spectra in frames (b)–(f). Red dotted spectra are for the filler $\varepsilon_f=1.82$ that immerses the {111} bands; blue dashed spectra are for the filler $\varepsilon_f=1.93$ that immerses the {220} bands.

having a frequency within the stop-band, exponentially decreases with travel distance within a PhC (see, e.g., Ref. 36). The dependence for the {111} band family is represented here as that of the (111) photonic band measured in the $\Gamma \rightarrow L_g$ geometry.

The experimental data indicate that the filler permittivity $\varepsilon_f^0(G_{111})=1.82$ determines the nondiffraction regime in both the (111) growth planes and the $(\bar{1}11)$ nongrowth planes, and this is valid for the $\Gamma \rightarrow L_g$ and $\Gamma \rightarrow K$ geometries, as well as for the whole range of wavelengths and wave vectors we have studied: the (A), (B), and (C) scans performed for the s and p polarizations (Sec. VI A).

2. {200} family, the nondiffraction regime at $\varepsilon_f^0(G_{200}) \sim 1.63$

The most convenient scattering geometry for observation of the {200} photonic bands is the wave vector range close to the $\Gamma \rightarrow X$ path (Figs. 6 and 7). In particular, the (A) scan shows the (200) band, with the respective wavelength at the point X ($\theta_A \approx -55°$) having the maximum value of ≈ 625 nm (for water-filled opals) only slightly exceeding the theoretical value for the {200} family, $\lambda_{\{200\}}(0) = 2d_{111}\sqrt{\varepsilon_{av}}\sqrt{3/4}=617$ nm. The (C) scan exhibits the (020) band at point X ($\theta_C=45°$) at ≈ 619 nm, which is also close to the theoretical value of $\lambda_{\{200\}}(0)$.

The immersion dependence of the (200) photonic band [Fig. 8(d)] demonstrates that this band is characteristic for all the fillers with the permittivity ε_f ranging from 1.78 (water) to 2.05 (propylene glycol). This result fully agrees with the data of Ref. 14. Figure 9 shows the dependence of the normalized (200) dip intensity on the filler permittivity ε_f. Keeping in mind the linear dependence for the (111) band and assuming a similar dependence for the (200) band, we can find the value of $\varepsilon_f^0(G_{200}) \sim 1.63$ at which the (200) photonic band is to be immersed by the filler.

The remarkable difference between the permittivity of the immersing filler, $\varepsilon_f^0(G_{200}) \sim 1.63$, and the average permittivity of the a-SiO_2 spheres, $\tilde{\varepsilon}_s=1.92$, is due to the fact that the reciprocal lattice vector modulus of this plane family, $G_{200}=8.886$, is simultaneously close to the special point $G_0 \approx 9.0$ at which the condition $\varepsilon_f^0(G) \equiv 0$ is valid and to the first resonance G_{res1} in the $\varepsilon_f^0(G)$ function for a low-contrast opal sample (see Fig. 3). It should be noted that the positions of the special G_0 points on the G scale are constant because the relation of Eq. (14) remains valid, irrespective of the dielectric parameters of the opal-filler structure.

3. {220} family, the nondiffraction regime at $\varepsilon_f^0(G_{220})=1.93$

In the (A) scan along the $L_g \rightarrow K_g \rightarrow L$ path, the (022) photonic band has the same energy as the (020) and (002) photonic bands, so it cannot be individually analyzed (Fig. 6). To separate these spectral bands, we should turn to the (B) $L_g \rightarrow W_g \rightarrow K$ scan in the $\Gamma L_g W_g K$ plane or to the (C) $K_g \rightarrow W_g \rightarrow X$ scan in the $\Gamma K_g W_g X$ plane normal to scan plane (A), i.e., $\Gamma L_g K_g L$. The degeneracy along these paths is removed, and the {200} and {220} families split, so that the

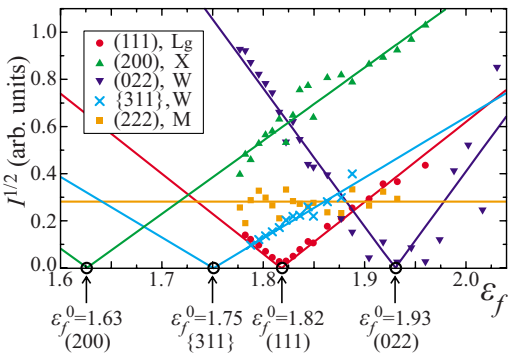

FIG. 9. (Color online) The normalized square root of the intensity of the (hkl) photonic bands as a function of the filler permittivity ε_f. Straight lines, the fitting of experimental points by a linear function.

respective wavelengths at the X point essentially differ: 619 nm for (020) and 370 nm for (022). The maximum wavelength $\lambda_{\{220\}}(0)=431$ nm lies at the K (K_g) points on the BZ surface. Note also that the (022) band in the (C) scan has a higher contrast in the p polarization. Thus, we have unambiguously separated the {200} and {220} photonic bands due to the comparison of experimental data and calculations as well as to the proper choice of the scanning paths.

The immersion dependence of the (022) band in the transmission spectra is shown in Fig. 8(c) for the $\Gamma \rightarrow K$ scattering geometry; the results of the spectral processing are presented in Fig. 9. Unlike the (111) and (200) photonic bands, the (022) band disappears at a much higher filler permittivity $\varepsilon_f^0(G_{220})=1.93$. This value agrees well with the value of 1.92 obtained in Ref. 14. In addition to the $\Gamma \rightarrow K$ scattering geometry, the {220} bands are observed along the $\Gamma \rightarrow W$ path (Fig. 6). The immersion dependence of this band family is given in Fig. 8(e) and the results are shown in Figs. 8(f) and 9. It is clearly seen that the {220} photonic bands become immersed at $\varepsilon_f^0(G_{220})=1.93$.

4. {311} family, the nondiffraction regime at $\varepsilon_f^0(G_{311})\sim 1.75$

The immersion dependence of the {311} photonic bands has never been studied before. To our knowledge, an experimental observation of these bands was reported in Refs. 19 and 40 only. The analysis of the band structure shown in Fig. 6 indicates that the best scattering geometry for the {311} photonic bands to be observed is the $\Gamma \rightarrow W_g$ path ($\theta_B \approx 40°$). The dispersion branches of the (311) and (131) bands intercept at the point W_g, and the calculation from formula (17) yields the value of 356 nm. It is important that the {311} branches do not intercept in the vicinity of this point with the dispersion branches of the other {hkl} band families (Fig. 6); therefore, the dips due to the {311} bands can be unambiguously attributed. Indeed, the transmission spectra taken along the $\Gamma \rightarrow W_g$ path contain a weak band centered at ~358 nm [Fig. 8(e)], which can be attributed to the {311} band family. Note also that the maximum theoretical wavelength for the {311} bands in our samples is found to be $\lambda_{\{311\}}(0)=372$ nm at $\theta_A \approx -30°$ and $\theta_B \approx 58°$ [$\lambda_{\{311\}}(0)=\sqrt{3/11}\lambda_{\{111\}}(0)$ for the ⟨311⟩ directions in the BZ]. However, the {311} bands are overlapped in these geometries by more intense bands of the other {hkl} families (Fig. 6), making the study of their immersion dependences impossible.

It is quite hard to understand the nature of the immersion dependence for the {311} band from the raw spectra in Fig. 8(e). However, the dependence of its integral intensity can be seen fairly well in Figs. 8(f). The {311} band exists for all of the fillers with a permittivity value of $1.78 \leq \varepsilon_f \leq 2.05$. Assuming a linear dependence of this band intensity similar to that of the (111) and (022) bands, we find the value of $\varepsilon_f^0(G_{311}) \sim 1.75$ at which the {311} photonic bands are to be immersed.

5. {222} family, the resonance photonic band without the nondiffraction regime

We have failed to find reports on the immersion dependence of the {222} photonic bands. The (222) bands are due to the second-order diffraction in the (111) growth planes and can be detected in the (A) and (B) scans at wavelengths $\lambda_{\{222\}}(\theta)$ twice as short as $\lambda_{\{111\}}(\theta)$ (Fig. 6). However, the (222) dispersion branch measured in the most convenient scattering geometry, $\Gamma \rightarrow L_g$, is superimposed on some other {hkl} branches, so it cannot be attributed exactly. For this reason, we used the $\Gamma \rightarrow M$ direction (see Sec. V B 1) to analyze the (222) band separately [Fig. 8(b)].

The processing results presented in Fig. 9 shows the normalized (222) dip intensity to be practically independent of the filler permittivity ε_f in the range $1.78 \leq \varepsilon_f \leq 2.05$. Therefore, we can attribute the {222} bands to the class of resonance photonic bands. The resonance nature of these bands is due to the fact that the reciprocal lattice vector modulus of these planes $G_{222}=2G_{111}=15.39$ lies in the region of the second resonance G_{res2} in the $\varepsilon_f^0(G)$ function for low-contrast opal (Fig. 3). Therefore, in spite of the second-order diffraction in the {111} growth planes, the {111} and {222} families demonstrate absolutely different immersion dependences. While the {111} photonic bands are immersed by a filler with $\varepsilon_f^0(G_{111})=1.82$, the {222} bands are not immersed in the ε_f range of interest and have the resonance nature or are similar to resonance bands, which can be immersed only by fillers with very high or very low (negative) permittivities $\varepsilon_f^0(G_{222})$.

C. Simulation of the $\varepsilon_f^0(G)$ function

Earlier, we simulated the general $\varepsilon_f^0(G)$ function by using formula (5) and two experimental parameters, $\varepsilon_f^0(G_{111})$ and $\varepsilon_f^0(G_{220})$.[14] The fitting parameters were the parameters of the rising piecewise linear function that modeled $\varepsilon_s(r)$. The choice of $\varepsilon_s(r)$ was based on the assumption that the smooth and continuous surface of a-SiO_2 spheres observed in the SEM images (Fig. 5) was an evidence for a higher density of the near-surface region, as compared to the porous nucleus.

In addition to the refined parameters $\varepsilon_f^0(G_{111})=1.82$ and $\varepsilon_f^0(G_{220})=1.93$, here we use two originally measured parameters, $\varepsilon_f^0(G_{200})=1.63$ and $\varepsilon_f^0(G_{311})=1.75$, as well the additional information about the value of $\varepsilon_f^0(G_{222})$ being close to the resonance value. A larger number of experimental points provide a higher reliability of the simulated permittivity $\varepsilon_s(r)$ of a-SiO_2 spheres. The permittivity value is further used to calculate the $\varepsilon_f^0(G)$ function from Eq. (5) and to compare its values with experimental $\varepsilon_f^0(G_{hkl})$. The simulation of $\varepsilon_s(r)$ was based on the TEM and SEM data (Fig. 5) indicating that the sphere surface of the experimental samples was continuous, so that it should have a permittivity close to that for bulk silica, $\varepsilon_{\alpha\text{-SiO}_2}=2.13$ (see the inset in Fig. 10). Further, Fig. 5 indicates that the dense shell has a small thickness as compared to the sphere radius and rapidly transforms to the porous nucleus. Taking these factors into account, we approximated the $\varepsilon_s(r)$ function with a piecewise linear function and employed nonlinear optimization procedures to calculate $\varepsilon_f^0(G)$, which describes the experimental data well (Fig. 10). The first two resonances of this function lie at $G_{\text{res1}}=9.07$ and $G_{\text{res2}}=15.54$. We would like to emphasize that the G_{res1} value is close to the reciprocal lattice vector modulus $G_{200}=8.886$ for the {200} bands, while the G_{res2} value is close to the reciprocal lattice vector moduli G_{311}

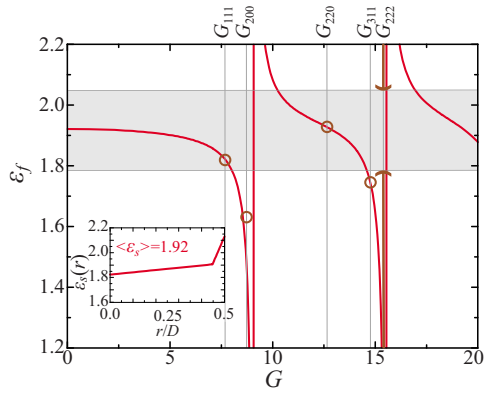

FIG. 10. (Color online) The nondiffraction conditions for an opal structure. The filler permittivity $\varepsilon_f^0(G)$ as a function of the reciprocal lattice vector calculated from Eq. (5) for the permittivity profile $\varepsilon_s(r)$ simulating the a-SiO_2 spheres. The $\varepsilon_s(r)$ profile is given in the inset. The moduli of the shortest reciprocal lattice vector G_{hkl} are shown by vertical lines. Circles, experimental values of $\varepsilon_f^0(G_{hkl})$.

$=14.735$ and $G_{222}=15.39$ for the two band families, {311} and {222}. This is the reason why the three band families cannot be immersed in the limited range of ε_f.

Figure 10 (see the insert) shows the model $\varepsilon_s(r)$ function obtained by the fitting, which can yield the average permittivity of the a-SiO_2 spheres. By averaging $\varepsilon_s(r)$ over the sphere volume, we get $\tilde{\varepsilon}_s=1.92$, a value which agrees fairly well with $\tilde{\varepsilon}_s=1.97$ derived from the processing of the reflection spectra for opals in Ref. 41. The value of $\tilde{\varepsilon}_s$ makes it possible to calculate the average permittivity of opal with a filler, $\varepsilon_{av}=0.74\tilde{\varepsilon}_s+0.26\varepsilon_f$, and is found to be $\varepsilon_{av}=1.88$ for water. Then, we use formula (17) and the experimental $\lambda_{(111)}$ values, measured with the highest possible accuracy among all sets of $\lambda_{(hkl)}$, to calculate the size of the a-SiO_2 spheres. The size we found, $D=317$ nm, is in perfect agreement with the earlier value of $D=315\pm15$ nm for the same opal sample.[25]

It should be mentioned that the averaged permittivity of spheres, $\tilde{\varepsilon}_s$, found earlier was identified with $\varepsilon_f^0(G_{111})$ at which the (111) dips are immersed.[21,39] The results of the present work directly show that these are quite different quantities: the average permittivity value $\tilde{\varepsilon}_s=1.92$ markedly differs from the immersion value $\varepsilon_f^0(G_{111})=1.82$.

VI. POTENTIAL APPLICATIONS

A. Selective switching of photonic bands: Active and passive modes

An obvious application of the effects discussed above is to selectively control the light fluxes of various wavelengths propagating through a crystal. Light is known to be the fastest information carrier, so future telecommunication circuits and computers can be based on elements made from photonic crystals. We believe that multi-component PhCs will become increasingly important in the near future due to a large variety of functions that can be governed by selective on/off switching.

Figure 7 demonstrates the selective on/off switching of photonic bands that can be performed either by a proper selection (modulation) of the crystal structural parameters (a) or by controlling the light polarization (b). The analysis of polarization features of photonic bands in low-contrast opals[25,26] demonstrated that each set of (hkl) crystal planes should be related to the respective the p and s components of linearly polarized light. The available data on light transmission[25,26] and diffraction[26] in opals indicate a certain similarity between the observable inhibition of photonic bands in the p polarization in a definite range of scanning angles and the classical effect in homogeneous media which defines the Brewster angle. In the case of PhCs, the quasi-Brewster angle $\theta^{qB}=a\tan\sqrt{\varepsilon_{av}/\varepsilon_v}$, where ε_{av} is the permittivity of the structure (in our case, the opal-filler system) and ε_v is the permittivity of the ambient (in our case, the filler).

Figure 11 summarizes the main results obtained in this study. It demonstrates, with reference to synthetic opals, the experimental dependence of the modulated photonic band structure of multi-component fcc PhCs on the permittivity of one of the components and on the linear polarization of the incident light. These results are given for samples filled with three materials: $\varepsilon_f=1.78$ (distilled water), $\varepsilon_f=2.05$ (propylene glycol), and $\varepsilon_f=\varepsilon_f^0(G_{111})=1.82$ (a mixture of water and propylene glycol). The p and s polarizations are defined respective to the scanning plane [(A), (B), or (C)].

One can see in Fig. 11 the complete switch-off effect for the {111} photonic bands at $\varepsilon_f=\varepsilon_f^0(G_{111})=1.82$. The {111} bands in this structure cannot be observed in any of the scattering geometries (that is for all the possible directions of the wave vector **K**): neither in the (111) growth planes nor in the $(\bar{1}11)$ nongrowth planes, in the whole spectral range of interest, 300–800 nm. We would like to stress that a theoretically perfect compensation of a photonic band in a wide spectral range is not feasible due to the difference in the dispersion dependences of the permittivity for silica, $\varepsilon_{a\text{-}SiO_2}(\lambda)$, and the filler, $\varepsilon_f(\lambda)$. However, our experiments have shown that this effect is not essential, so it will not be discussed here. In addition to the dispersion dependence, Fig. 11 demonstrates the polarization dependence of the photonic band structure, which reveals itself at the quasi-Brewster angle θ^{qB} individually defined for each (hkl) plane family.

Therefore, the multi-component nature of PhCs may open opportunities to photonics. Indeed, a common two-component PhC can exist only in two states: (1) in the off state when all of its photonic bands are open ($\varepsilon_f\neq\varepsilon_s$, the incident beam is reflected) or (2) in the on state when all the bands are closed ($\varepsilon_f=\varepsilon_s$, the incident beam is transmitted). For this reason, a two-component PhC does not allow independent information processing by using different Bragg wavelengths $\lambda_{(hkl)}$. In contrast, a multi-component PhC is capable to switch on/off photonic bands, thereby selectively creating several possible states. Clearly, the latter type of crystals possesses much greater communication capabilities and can be employed as selective switches and selective waveguides in various optoelectronic devices.

Selective processing of signals can be performed in the passive or dynamic mode. The passive mode uses a multi-component PhC with prescribed parameters $\varepsilon_f^0(G_{hkl})$, which

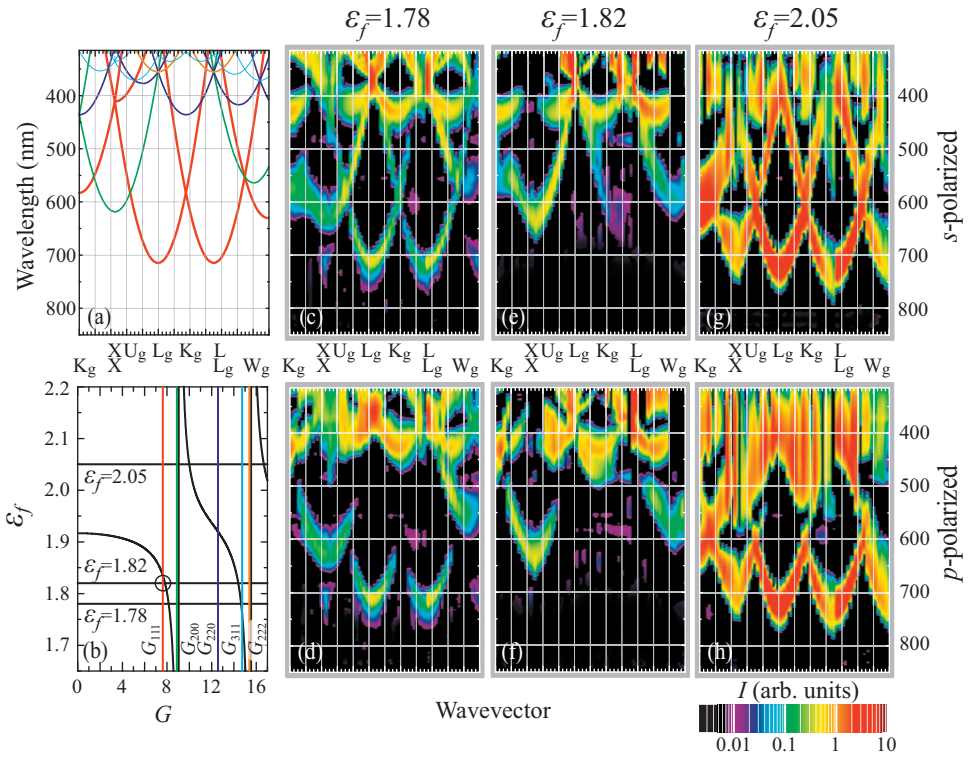

FIG. 11. (Color) The photonic band structure of opal. (a) Bragg wavelengths vs the angle of incidence for diffraction from different $\{hkl\}$ plane families calculated from Eq. (18) for three scanning paths [(A)–(C)], Eq. (17). The calculation parameters are the same as in Fig. 6. Red lines, the {111} family of planes; green, {200}; blue, {220}; cyan, {311}; orange, {222}. (b) The filler permittivity $\varepsilon_f^0(G)$ in the nondiffraction regime (black line) calculated from Eq. (5) for the permittivity profile $\varepsilon_s(r)$ shown in Fig. 10. The filler permittivity values ε_f=1.78, 1.82, and 2.05 are shown by horizontal lines. The moduli of the shortest reciprocal lattice vector G_{hkl} are given by vertical lines. [(c)–(h)] The photonic band structure of opals for three fillers and two linear polarizations is shown on the same scales of wavelengths and wave vectors and in the same scanning planes as the calculations in frame (a). The intensity scale of photonic bands is given in the lower right corner. (c) ε_f=1.78, *s* polarization, (d) ε_f=1.78, *p* polarization, (e) ε_f=1.82, *s* polarization, (f) ε_f=1.82, *p* polarization, (g) ε_f=2.05, *s* polarization, and (h) ε_f=2.05, *p* polarization.

separates in space (reflects or transmits) the information propagating at different Bragg wavelengths $\lambda_{(hkl)}$. Greater perspectives are provided by the time modulation of the crystal parameters, which can allow a selective manipulation of the information transmitted at various Bragg wavelengths $\lambda_{(hkl)}$ in the online mode. The on/off selective switching can be realized by dynamic tuning of the permittivity of one (or several) component(s)[22,23] or by picosecond strain pulses,[42] i.e., by modulation of the reciprocal lattice vector G. The modulation can be particularly effective near the resonance point ($G \sim G_{\text{res}}$) at the Bragg wavelengths $\lambda_{(200)}$.

To summarize, we identified the following stop-bands' switching mechanisms:

(i) Selective polarization mechanism based on a quasi Brewster effect. In contrast to other mechanisms, it is not related to a scattering form factor $S(G)$ becoming zero. For the light propagating at a critical incident angle θ^{qB} to the planes (hkl), the corresponding (hkl) stop-band disappears in *p* polarization and remains constant in *s* polarization. This effect can be observed in both the two-component and multi-component PCs.

(ii) Nonselective mechanism that may be observed only in two-component PCs and is related to the formation of optically uniform material when the dielectric contrast between the matrix and filler completely disappears. The effect could be achieved by varying the permittivity of one component. In this case, all of the photonic stop-bands $\{hkl\}$ disappear at the same time as the scattering form factor $S(G) \equiv 0$ for all the **G** vectors.

(iii) Selective mechanism that takes place when $S(G_{hkl}=0)$ by varying one of the structural parameters of PCs. The effect can be observed in both the two-component and multi-component PCs.

(iv) Selective mechanism that takes place when $S(G_{hkl})=0$ by varying one of the dielectric parameters of PCs. The effect can only be observed in multi-component PCs. The experimental and theoretical study of this effect first observed in Ref. 14 was the main focus of our investigation.

B. Optical cloaking of periodic nanostructures

Another potential application of the effects discussed above is related to "cloaking," which was a subject active interest in recent years.[43–46] The problem is how to make a region in space classically opaque or transparent to waves in the whole or, at least, partial spectral range. In perfect causal cloaking, waves must appear to pass through an object as if it is an empty space or a transparent media.

Because every material has a local response, there is no material that could be used as an "invisible paint" for genuine cloaking. Recent reports have shown that a shell of metamaterial could achieve cloaking but only to monochromatic electromagnetic waves.[44,45] As an alternative to cloaking with a metamaterial, a method was proposed which is based on wave measurement and final wave cancellation.[46] In this method, special sensors would measure the waves near the surface of the object and excite active sources of electromagnetic waves using an approach to determine those sources. Note that active sources cloaking for slowly propagating acoustic waves have no problems in principle,[47,48] although cloaking to broadband optical waves is problematic because there is little or no time available for any calculations or extra propagation.[46]

The results presented above seem to be closely related to these problems and can be regarded as steps on the way to cloaking technologies for periodic structures. Two-component structures become fully transparent to light when the permittivity of one component matches that of the other. Full light transparency is impossible to create in multi-component periodic structures, but they can be made transparent to certain wavelengths in certain directions. Indeed, the technique we have suggested allows selection of such a homogeneous medium with constant permittivity ε_f for any inhomogeneous sphere profile $\varepsilon_s(r)$ that the resultant structure becomes optically transparent to waves in a definite wavelength range. This kind of structure can be considered as being totally opaque, with only one structural element being "visible."

In particular, at $\varepsilon_f=\varepsilon_f^0(G_{111})$, we immerse the {111} family of bands, thereby considerably broadening the opacity range and shifting the red diffraction cutoff toward the shorter wavelength region. In this case, the red diffraction cutoff of the whole periodic structure, which is determined in the fcc lattice by the diffraction boundary of the {111} planes, $\lambda_{\{111\}}(0)=2d_{111}\sqrt{\varepsilon_{\mathrm{av}}}$, is shifted to the diffraction boundary of the {200} planes, $\lambda_{\{200\}}(0)=\sqrt{3/4}\lambda_{\{111\}}(0)$. Therefore, the spectral range between $\lambda_{\{111\}}(0)$ and $\lambda_{\{200\}}(0)$ becomes fully transparent in any direction in the lattice, as is well seen in Fig. 11. Thus, we have given an example of collective cloaking of a multitude of identical particles in the chosen wavelength range.

VII. CONCLUSION

We reported on a detailed study of switching off {*hkl*} stop-bands depending on the structural and dielectric parameters of PhCs, as well as on the polarization of the incoming light. The suggested classification of PhCs as *two-component* PhCs and *multi-component* ones was found to play an important role in distinguishing the stop-bands' switching mechanisms. We showed that the Bragg diffraction on the nonresonance {*hkl*} planes in multi-component periodic structures can be selectively switched off, with each {*hkl*} plane family being immersed at the intrinsic permittivity $\varepsilon_f^0(G_{hkl})$ of the variable component of this structure. In other words, the immersion permittivity value splits on the ε scale. In the resonance planes, however, the Bragg diffraction cannot be switched off by changing the permittivity of one of the components. This medium can never be transparent to the respective Bragg wavelengths λ_{Bragg}.

These effects were theoretically treated with reference to Bragg diffraction in multi-component photonic crystals and experimentally studied from light transmission spectra of 3D opal-filler systems. One should keep in mind that many photonic crystals known today are multi-component structures. For example, there are no natural or synthetic opals made up of homogeneous spheres, they are just theoretical models. Inhomogeneities of a-SiO_2 spheres, which seem inessential at first sight, may lead to remarkable optical effects, some of which were studied in the present work. Various semiconductor 2D photonic crystals have a complex space-periodic morphology and a defect surface formed during their fabrication by lithographic techniques. Generally, multi-component photonic crystals can be produced by sputtering or deposition of various compounds on host structures. Here, we have described the methods we used for the calculation of photonic characteristics of such compounds and showed that a proper selection of structural and dielectric parameters can always lead to a resonance photonic band. Similarly, one can selectively switch off the prescribed photonic bands splitted on the permittivity scale. It is important that some photonic bands that cannot be switched off by immersion in the accessible permittivity range (e.g., the {200} bands) can be manipulated by using the properly chosen incident light polarization.

We used optical transmission spectroscopy to experimentally study the photonic band gap of opals as a function of the filler permittivity, light polarization, and incident beam orientation in the fcc lattice. The measurements were made for all high-symmetry points and directions across the Brillouin zone. The conventional model of synthetic opals as a two-component composite was found to be inadequate to describe their photonic properties. We analyze this problem and demonstrated that the microstructure of a-SiO_2 spheres needs to be taken into account and that opals should be regarded as multi-component photonic crystals. The experimental data and calculations presented here demonstrate a very good agreement.

To conclude, we can expect a variety of new effects in multi-component photonic crystals and their potential applications. These effects can be used to design new types of PhC-based devices. Since the structure permittivity can be deliberately controlled, it would not be hard to design multi-component PhCs that would exhibit different nondiffraction states of preselected {*hkl*} photonic bands in the passive mode. Dynamic modulation of the permittivity or the lattice parameters may allow a selective on/off switching of desired (*hkl*) bands and, as a result, provide a simultaneous control of the information transmitted at different wavelengths in the online mode.

ACKNOWLEDGMENTS

We thank A. A. Kaplyanskii and V. A. Kosobukin for helpful discussions and M. I. Samoylovich and A.V. Guryanov for the preparation of the samples. SEM was performed

in the Centralized Materials Characterization Facility of A. J. Drexel Nanotechnology Institute. TEM studies were done in the Penn Regional Nanotechnology Facility, University of Pennsylvania. This work was supported in part by the Super Optical Information Memory Project from the Ministry of Education, Culture, Sports, Science and Technology of Japan (MEXT), Grant-in-Aid for Scientific Research (S) No. 17106004 from Japan Society for the Promotion of Science (JSPS), and by the RFBR Grant No. 08-02-00642.

[1] E. Yablonovitch, Phys. Rev. Lett. **58**, 2059 (1987).
[2] S. John, Phys. Rev. Lett. **58**, 2486 (1987).
[3] J. D. Joannopoulos, R. D. Meade, and J. N. Winn, *Photonic Crystals: Molding the Flow of Light* (Princeton University, Princeton, NJ, 1995).
[4] *Photonic Crystals: Physics, Fabrication and Applications*, edited by K. Inoue and K. Ohtaka (Springer, New York, 2004).
[5] K. Sakoda, *Optical Properties of Photonic Crystals*, 2nd ed. (Springer, New York, 2004).
[6] E. Yablonovitch, J. Phys.: Condens. Matter **5**, 2443 (1993).
[7] A. Guinier, *Crystals, Imperfect Crystals, and Amorphous Bodies* (Freeman, San Francisco, 1963).
[8] K. M. Ho, C. T. Chan, and C. M. Soukoulis, Phys. Rev. Lett. **65**, 3152 (1990).
[9] H. S. Sözüer, J. W. Haus, and R. Inguva, Phys. Rev. B **45**, 13962 (1992).
[10] K. Busch and S. John, Phys. Rev. E **58**, 3896 (1998).
[11] H. Takeda and K. Yoshino, Appl. Phys. Lett. **80**, 4495 (2002).
[12] P. D. García, J. F. Galisteo-López, and C. López, Appl. Phys. Lett. **87**, 201109 (2005).
[13] A. Glushko and L. Karachevtseva, Photonics Nanostruct. Fundam. Appl. **4**, 141 (2006).
[14] A. V. Baryshev, A. B. Khanikaev, M. Inoue, P. B. Lim, A. V. Sel'kin, G. Yushin, and M. F. Limonov, Phys. Rev. Lett. **99**, 063906 (2007).
[15] P. J. Darragh, A. J. Gaskin, B. C. Terrell, and J. V. Sanders, Nature (London) **209**, 13 (1966).
[16] R. K. Iler, *The Chemistry of Silica* (Wiley, New York, 1979).
[17] W. Stöber, A. Fink, and E. Bohn, J. Colloid Interface Sci. **26**, 62 (1968).
[18] P. J. Darragh and J. L. Perdrix, J. Gemmol.. **14**, 215 (1975).
[19] M. V. Rybin, K. B. Samusev, and M. F. Limonov, Photonics Nanostruct. Fundam. Appl. **5**, 119 (2007).
[20] V. N. Astratov, V. N. Bogomolov, A. A. Kaplyanskii, A. V. Prokofiev, L. A. Samoilovich, S. M. Samoilovich, and Yu. A. Vlasov, Nuovo Cimento D **17**, 1349 (1995).
[21] Yu. A. Vlasov, V. N. Astratov, O. Z. Karimov, A. A. Kaplyanskii, V. N. Bogomolov, and A. V. Prokofiev, Phys. Rev. B **55**, R13357 (1997).
[22] D. A. Mazurenko, R. Kerst, J. I. Dijkhuis, A. V. Akimov, V. G. Golubev, D. A. Kurdyukov, A. B. Pevtsov, and A. V. Sel'kin, Phys. Rev. Lett. **91**, 213903 (2003).
[23] A. B. Pevtsov, D. A. Kurdyukov, V. G. Golubev, A. V. Akimov, A. A. Meluchev, A. V. Sel'kin, A. A. Kaplyanskii, D. R. Yakovlev, and M. Bayer, Phys. Rev. B **75**, 153101 (2007).
[24] A. V. Baryshev, A. A. Kaplyanskii, V. A. Kosobukin, K. B. Samusev, D. E. Usvyat, and M. F. Limonov, Phys. Rev. B **70**, 113104 (2004).
[25] A. V. Baryshev, A. B. Khanikaev, H. Uchida, M. Inoue, and M. F. Limonov, Phys. Rev. B **73**, 033103 (2006).
[26] M. V. Rybin, A. V. Baryshev, M. Inoue, A. A. Kaplyanskii, V. A. Kosobukin, M. F. Limonov, A. K. Samusev, and A. V. Sel'kin, Photonics Nanostruct. Fundam. Appl. **4**, 146 (2006).
[27] B. T. Holland, C. F. Blanford, and A. Stein, Science **281**, 538 (1998).
[28] J. E. G. J. Wijnhoven and W. L. Vos, Science **281**, 802 (1998).
[29] A. A. Zakhidov, R. H. Baughman, Z. Iqbal, C. Cui, I. Khairulin, S. O. Dantas, J. Marti, and V. G. Ralchenko, Science **282**, 897 (1998).
[30] M. S. Thijssen, R. Sprik, J. E. G. J. Wijnhoven, M. Megens, and T. Narayanan, Ad Lagendijk, and W. L. Vos, Phys. Rev. Lett. **83**, 2730 (1999).
[31] S. G. Romanov, T. Maka, C. M. Sotomayor Torres, M. Muller, R. Zentel, D. Cassagne, J. Manzanares-Martinez, and C. Jouanin, Phys. Rev. E **63**, 056603 (2001).
[32] A. V. Baryshev, A. A. Kaplyanski, V. A. Kosobukin, M. F. Limonov, and A. P. Skvortsov, Phys. Solid State **46**, 1331 (2004).
[33] A. V. Baryshev, V. A. Kosobukin, K. B. Samusev, D. V. Usvyat, and M. F. Limonov, Phys. Rev. B **73**, 205118 (2006); Phys. Solid State **45**, 459 (2003).
[34] A. Yariv and P. Yeh, *Optical Waves in Crystals* (Wiley, New York, 1984).
[35] A. Modinos, N. Stefanou, I. E. Psarobas, and V. Yannopapas, Physica B (Amsterdam) **296**, 167 (2001).
[36] Yu. A. Vlasov, M. A. Kaliteevski, and V. V. Nikolaev, Phys. Rev. B **60**, 1555 (1999).
[37] A. A. Chabanov, Y. Jun, and D. J. Norris, Appl. Phys. Lett. **84**, 3573 (2004).
[38] V. N. Bogomolov, L. M. Sorokin, D. A. Kurdyukov, T. M. Pavlova, and J. L. Hutchison, Phys. Solid State **39**, 1869 (1997).
[39] M. V. Rybin, K. B. Samusev, and M. F. Limonov, Phys. Solid State **49**, 2280 (2007).
[40] S. A. Asher, J. M. Weissman, A. Tikhonov, R. D. Coalson, and R. Kesavamoorthy, Phys. Rev. E **69**, 066619 (2004).
[41] O. A. Kavtreva, A. V. Ankudinov, A. G. Bazhenova, Yu. A. Kumzerov, M. F. Limonov, K. B. Samusev, and A. V. Sel'kin, Phys. Solid State **49**, 708 (2007).
[42] Y. Tanaka, S.-I. Tamura, A. Akimov, A. Pevtsov, S. Kaplan, A. Dukin, V. Golubev, D. Yakovlev, and M. Bayer, J. Phys.: Conf. Ser. **92**, 012107 (2007).
[43] A. Alu and N. Engheta, Phys. Rev. E **72**, 016623 (2005).
[44] U. Leonhardt, Science **312**, 1777 (2006).
[45] J. B. Pendry, D. Schurig, and D. R. Smith, Science **312**, 1780 (2006).
[46] D. A. B. Miller, Opt. Express **14**, 12457 (2006).
[47] P. A. Nelson and S. J. Elliott, *Active Control of Sound* (Academic, London, 1992), pp. 290–293.
[48] E. Friot, R. Guillermin, and M. Winninger, Acta Acust. **92**, 278 (2006).